Research on Oscillation of Turbo-generator and MMC-HVDC Interconnection System

Jialong Li, Xinyu Lu, Xiong Du, *Member*, *IEEE*, Junliang Liu, and Lijuan Fan

***Abstract*—The rapid advancement of modular multilevel converter-based high-voltage direct current (MMC-HVDC) interconnection projects may lead to torsional vibrations in turbo-generator shafts, causing oscillations that pose operational risks to the power system. Impedance-based analysis is an effective method to evaluate the stability of power systems with power electronic components. However, conventional turbo-generator impedance models, such as the RL equivalent impedance model, only address the electrical aspects of turbo-generators and neglect the influence of shafting characteristics, potentially leading to inaccurate analysis results. To address this issue, a turbo-generator impedance model is introduced which incorporates shafting characteristics validated through frequency scanning methods. Focusing on the turbo-generator and MMC-HVDC interconnection system, the oscillation analysis results are compared using the developed and traditional impedance models. The findings indicate that the developed model exhibits greater applicability and accuracy for power systems incorporating electronic equipment. Furthermore, a virtual damping control strategy for MMC-HVDC based on modulation links is developed to mitigate oscillation issues. The efficacies of the proposed impedance model and control strategy are validated in the turbo-generator and MMC-HVDC interconnection system.**

***Index Terms*—Impedance model, turbo-generator, shafting torsional vibration, MMC-HVDC interconnection system, oscillation suppression.**

I. Introduction

The emergence of modular multilevel converter-based high-voltage direct current (MMC-HVDC) systems addresses issues related to high switching frequency and high power losses in two-level converter based systems [1]. Its advantages, including low output voltage harmonic content, high waveform quality, and low switching losses, have led to widespread adoption in engineering applications [2], [3]. For instance, prominent flexible interconnection projects in China, such as the Chongqing-Hubei back-to-back DC and Zhangbei projects, all employ MMC topology [4]–[6]. However, in scenarios where thermal power units are located near MMC-HVDC converter stations and the electrical distance is relatively short, torsional vibrations in turbo-generator shafting may occur, potentially causing sub-synchronous oscillations in the power system. Historically, the issue of sub-synchronous oscillations in turbo-generators was primarily manifested in series compensation transmission systems and LCC-HVDC transmission systems, originated from the swift response of the DC control system. For example, the Square Butte Power Plant in the United States and the Hami, Suizhong, and Yimin Power Plants in China faced risks of sub-/super-synchronous oscillations owing to LCC-HVDC integration [7]–[10]. Similarly, characterized by their rapid response, MMC-HVDC systems may pose sub-synchronous oscillation risks when thermal power units are located near the converter stations. In China, the 14th Five-Year Plan encompasses the development of an MMC-HVDC-based flexible interconnection project near a thermal power plant in Guangdong Province's Pearl River Delta region. Therefore, it is crucial to promptly assess the risk of sub-synchronous oscillations and perform research on mitigating oscillations in the turbo-generator and MMC-HVDC interconnection system.

The rapid expansion of HVDC interconnection systems, and notably MMC-HVDC, leads to increasingly complex structural challenges in power systems [11]–[14]. The state-space and complex torque coefficient methods are widely used to analyze system stability in this context. However, the order of the state-space model tends to increase, potentially restricting its applicability in larger systems [15]. Moreover, the complex torque coefficient method may struggle to accurately identify all electromechanical oscillation states or provide accurate damping values for oscillation modes [16]. In contrast to the abovementioned methods, the impedance-based analysis method offers modularity and scalability in the framework of electric power systems, making it an effective tool for analyzing systems with complex structures [17]. Estab-

Received: September 13, 2024
Accepted: February 25, 2025
Published Online: September 1, 2025
Jialong Li, Xinyu Lu, Xiong Du (corresponding author), and Junliang Liu are with the School of Electrical Engineering, Chongqing University, Chongqing 400044, China (e-mail: lijialong@163.com; 20191113100t@cqu.edu.cn; duxiong@cqu.edu.cn; ljl@cqu.edu.cn).
Lijuan Fan is with the System Research Institute of CSG, Guangzhou 518000, China (e-mail: fanlj03@163.com).
DOI: 10.23919/PCMP.2024.000009

lishing an impedance model plays a critical role in leveraging this method. However, there lacks research on the impedance model of turbo-generators. Typically, turbo-generator impedance is approximated using RL series impedance or equivalent circuit impedance of synchronous generators [18], [19], which fails to capture the unique shafting characteristics of turbo-generators. Therefore, the influence of turbo-generator shafting on sub-/super-synchronous oscillations in the system cannot be adequately analyzed, potentially resulting in inaccurate conclusions near the natural torsional vibration frequency. Consequently, there is an urgent need for an accurate impedance model of turbo-generators owing to the rapid proliferation of power electronic equipment and the increasingly complex power system structures.

This study primarily elucidates the following aspects.

1) An impedance model of the turbo-generator that incorporates torsional characteristics of the shafting is developed, addressing the current limitation where existing models only account for electrical characteristics without considering mechanical aspects.

2) A case study is presented to illustrate sub-synchronous oscillations in a turbo-generator and MMC-HVDC interconnection system. The impedance model introduced in this study is analyzed and compared with traditional models, confirming its accuracy in the sub-synchronous frequency range.

3) An adaptive virtual damping control strategy based on modulation links is proposed to enhance damping in MMC-HVDC systems and effectively suppress sub-synchronous oscillations.

II. Turbo-generator and MMC-HVDC Interconnection System

This study focuses on the hybrid system comprising a turbo-generator and MMC-HVDC interconnection system, depicted in Fig. 1. The turbo-generator structure and parameters are based on actual data from a thermal power plant in Guangdong province. In Fig. 1, HP, IP, and LP are high, medium, and low-pressure cylinders, respectively; while GEN is the synchronous generator; the transformer ratios for the turbo-generator and MMC are 22/500 kV and 500/270 kV, respectively; R_{L} and X_{L} are the line resistance and inductive reactance; while R_{g} and X_{g} are the grid resistance and inductive reactance.

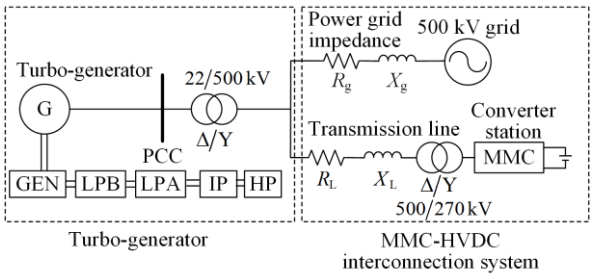

Fig. 1. Diagram of turbo-generator and MMC-HVDC interconnection system.

In this study, the impedance model of the turbo-generator depicted within the dashed lines on the left of Fig. 1 is established. This model enables sub-/super-synchronous oscillation analysis in conjunction with the MMC-HVDC interconnection system. The impedance model diagram of the turbo-generator and the MMC-HVDC interconnection system is illustrated in Fig. 2.

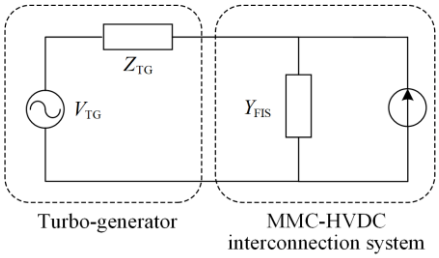

Fig. 2. Diagram of the impedance model of the turbo-generator and MMC-HVDC interconnection system.

The impedance model of MMC has already been comprehensively studied [20]. Thus, the focal point of impedance analysis for the interconnection system is to accurately calculate the turbo-generator impedance (Z_{TG}). The sequence impedance model Z_{TG} of the turbo-generator, accounting for shafting characteristics, is expressed in (1). The detailed derivation of the impedance formula for Z_{TG} is presented in Section III.

$$\begin{bmatrix}\Delta u_{\mathrm{p}}(\omega_{\mathrm{p}})\\ \Delta u_{\mathrm{n}}(\omega_{\mathrm{p}})\end{bmatrix}=\begin{bmatrix}Z_{\mathrm{TG\_pp}}(\omega_{\mathrm{p}}) & Z_{\mathrm{TG\_pn}}(\omega_{\mathrm{p}})\\ Z_{\mathrm{TG\_np}}(\omega_{\mathrm{p}}) & Z_{\mathrm{TG\_nn}}(\omega_{\mathrm{p}})\end{bmatrix}\begin{bmatrix}\Delta i_{\mathrm{p}}(\omega_{\mathrm{p}})\\ \Delta i_{\mathrm{n}}(\omega_{\mathrm{p}})\end{bmatrix} \quad (1)$$

The MMC impedance model is presented in (2) [20], and the parameter settings are shown in Table I.

TABLE I
Parameters of the MMC System

Symbol	Parameter	Value
L (mH)	Bridge arm inductance	75
R (Ω_r)	Bridge arm resistance	0.1
N (piece)	Number of sub-modules	244
C_{S} (mF)	Submodule capacitance	15
V_{dc} (kV)	Rated voltage at DC side	500
V_{ac} (kV)	Rated voltage at AC side	270
H_{P}	Active power controller	$2\times10^{-7}+2\times10^{-6}/s$
H_{Q}	Reactive power controller	$-2\times10^{-7}-2\times10^{-6}/s$
H_{i}	Current inner loop controller	$5+150/s$
H_{ic}	Circulation controller	$50+200/s$
H_{pll}	Phase locked loop	$(0.0013+0.145/s)/s$
P (MW)	Transmission power	800

$$\boldsymbol{Z}_{\mathrm{MMC}}(\omega_{\mathrm{p}})=\begin{bmatrix}Z_{\mathrm{MMC\_pp}}(\omega_{\mathrm{p}}) & Z_{\mathrm{MMC\_pn}}(\omega_{\mathrm{p}})\\ Z_{\mathrm{MMC\_np}}(\omega_{\mathrm{p}}) & Z_{\mathrm{MMC\_nn}}(\omega_{\mathrm{p}})\end{bmatrix} \quad (2)$$

where $Z_{\mathrm{MMC\_pp}}(\omega_{\mathrm{p}})$ and $Z_{\mathrm{MMC\_pn}}(\omega_{\mathrm{p}})$ denote the self and mutual impedances of the MMC converter, respectively.

Subsequently, the impedance model of the MMC-HVDC interconnection system on the right side

of the PCC can be formulated with reference to Fig. 1. Its small-signal equivalent circuit is depicted in Fig. 3, and accordingly, the MMC-HVDC interconnection system impedance can be calculated, as shown in Eq. (A1) in Appendix A .

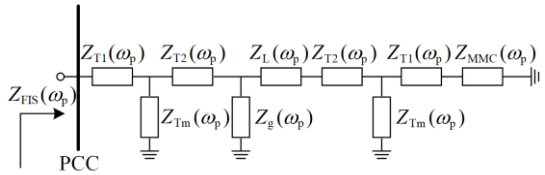

Fig. 3. Small-signal equivalent circuit of the MMC-HVDC interconnection system.

In Fig. 3, $Z_{T1}(\omega_p)$, $Z_{T2}(\omega_p)$ and $Z_{Tm}(\omega_p)$ represent the impedances of the high-voltage side, low-voltage side, and excitation of the transformer, respectively. $Z_L(\omega_p)$ denotes the line impedance, and $Z_g(\omega_p)$ represents the impedance in the power grid. K_1 and K_2 in Eq.(A1) denote the transformer turns ratios of 22/500 kV and 270/500 kV on the turbo-generator and MMC sides, respectively.

III. Impedance Modeling of Turbo-generator Considering Shafting Characteristics

The traditional impedance model of a turbo-generator typically only considers its electrical characteristics and is equivalent to the impedance model of a synchronous generator [18], [19]. The impedance model developed in this study for the turbo-generator emphasizes mechanical characteristics such as governor and shafting spring models. This approach enables a more accurate characterization of the turbo-generator impedance characteristics in the sub-synchronous frequency band.

This discussion does not address the linearized small-signal model of the synchronous generator. Its voltage and excitation equations are depicted in (A2) and (A3). The small-signal equation of the synchronous generator can be derived by combining these equations, shown as:

$$\Delta \boldsymbol{U} = (\boldsymbol{R} + \frac{s}{\omega_0}\boldsymbol{X} - \boldsymbol{W}_0)\Delta \boldsymbol{I} - \boldsymbol{\psi}_0 \Delta\omega_1 \tag{3}$$

where $\Delta \boldsymbol{U}$ and $\Delta \boldsymbol{I}$ denote the small disturbance voltage and current vectors of the stator windings, excitation windings, and damping windings of the *d*-axis and *q*-axis; $\boldsymbol{R}$ and $\boldsymbol{X}$ represent the resistance and reactance matrices in (A2) and (A3); while $\boldsymbol{W}_0\Delta \boldsymbol{I}$ and $\boldsymbol{\psi}_0\Delta\omega_1$ represent the two components resulting from the linearization of small signals related to flux linkage and rotor speed coupling terms.

Examining (3), we observe that the relationship between $\Delta \boldsymbol{U}$ and $\Delta \boldsymbol{I}$ can be established by eliminating $\Delta\omega_1$, which connects the electrical component with the mechanical component of the shafting. The next step involves modeling the mechanical structure of each part of the shafting.

A. Shafting

The shafting system is divided into five shaft sections, with the synchronous generator designated as the first mass block, followed by the low-pressure and high-pressure cylinders. The schematic diagram of the shaft mass-spring model is illustrated in Fig. 4 [21].

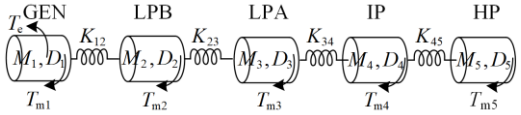

Fig. 4. Schematic diagram of the turbo-generator shafting mass-spring model.

The linearized equation for the small signal of the shafting system is:

$$\begin{cases} s\Delta\delta_i = \Delta\omega_i, \quad i = 1,2,3,4,5 \\ s\Delta\omega_i = \dfrac{1}{M_i}\Big[\Delta T_{mi} - D_{i,i}\Delta\omega_i - K_{i,i+1}(\Delta\delta_i - \Delta\delta_{i+1}) - \\ \qquad K_{i-1,i}(\Delta\delta_i - \Delta\delta_{i-1})\Big] \end{cases} \tag{4}$$

where δ_i is the electrical twist angle of the *i*th mass block of the shafting relative to the synchronous rotation reference axis; M_i is the inertia coefficient of the *i*th mass block; K_{ij} is the elastic coefficient between the mass blocks; D_i is the self-damping coefficient of the *i*th mass block of the steam turbine; and T_{mi} is the mechanical torque of the mass block. Mass block 1 corresponds to the rotor shaft section of the synchronous generator. Thus, $T_1 = -T_e$, where T_e is the electromagnetic torque, expressed as:

$$\Delta T_e = i_{q0}\Delta\psi_d + \psi_{d0}\Delta i_q - i_{d0}\Delta\psi_q - \psi_{q0}\Delta i_d \tag{5}$$

The shafting parameters of the turbo-generator are obtained from a thermal power plant in Guangdong province, as shown in Table II.

TABLE II
Turbo-generator Shafting Parameters

Mass	Inertia (kg·m²)	Spring constant (N·m/rad)	Damping (N·m·s/rad)
HP	7.051 95×10³	2.920 94×10⁷ (HP-IP)	364.7562
IP	2.358 76×10⁴	6.278 85×10⁷ (IP-LPA)	60.7927
LPA	2.030 48×10⁴	8.041 27×10⁷ (LPA-LPB)	60.7927
LPB	2.226 23×10⁴	1.352 10×10⁸ (LPB-GEN)	1215.854
GEN	1.151 41×10⁴		0

B. Steam Turbine

The turbo-generator examined in this study features four pressure cylinders, requiring the adoption of a third-order turbine mathematical model. The block diagram illustrating the transfer function is depicted in Fig. 5.

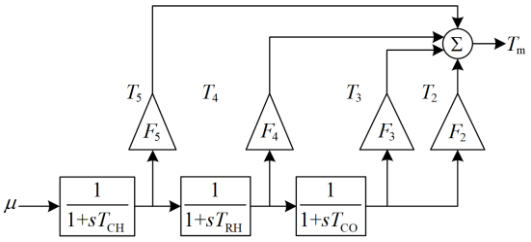

Fig. 5. Block diagram depicting the transfer function of the steam turbine.

As shown in Fig. 5, the steam turbine's input is the governor-controlled valve opening μ; T_{CH} and T_{RH} are the time constants of the high-pressure chamber and intermediate reheat pipe, respectively; T_{CO} is the time constant across the tubes; while F_5, F_4, F_3, and F_2 are the mechanical power ratios of the cylinders in high, medium, and low-pressure stages, respectively, with their sum equaling 1. In this study, a power distribution ratio of $F_5:F_4:F_3:F_2=0.3:0.26:0.22:0.22$ is used. Based on the transfer block diagram, the linearized small-signal equation for steam turbine is derived as:

$$\begin{cases} -F_2\Delta T_4+(F_4+F_4T_{CO}s)\Delta T_2=0 \\ -F_3\Delta T_4+(F_4+F_4T_{CO}s)\Delta T_3=0 \\ -F_4\Delta T_5+(F_5+F_5T_{RH}s)\Delta T_4=0 \\ -F_5\Delta\mu+(1+T_{CH}s)\Delta T_5=0 \end{cases} \tag{6}$$

C. Governor

In this study, we use a hydraulic governor without the limiter for control, and the control block diagram is depicted in Fig. 6.

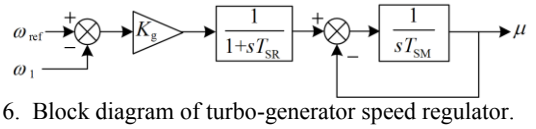

Fig. 6. Block diagram of turbo-generator speed regulator.

As shown in Fig. 6, ω_1 and ω_{ref} are the actual and reference rotor speeds of the synchronous generator, respectively; α is the intermediate variable of the inertia link output; K_g is the governor's amplification factor; T_{SM} is the integration time constant of the oil engine; and T_{SR} is the first-order inertia link of the relay. Subsequently, the small-signal linearization equation of the speed regulator is expressed as:

$$\begin{cases} (1+T_{SR}s)\Delta\alpha+K_g\Delta\omega_1=0 \\ -\Delta\alpha+(1+T_{SM}s)\Delta\mu=0 \end{cases} \tag{7}$$

D. Impedance Model of Turbo-generator and Verification

At this point, the small-signal linearization equation of the turbo-generator can be derived by combining (3)–(7) as follows:

$$\boldsymbol{A}\Delta\boldsymbol{y}=\Delta\boldsymbol{u} \tag{8}$$

The matrices $\Delta\boldsymbol{y}$ and $\Delta\boldsymbol{u}$ are shown in (A4). Then, the relationship between $\Delta\boldsymbol{u}$ and $\Delta\boldsymbol{i}$ is obtained as:

$$\begin{bmatrix}\Delta u_d\\ \Delta u_q\end{bmatrix}=Z_{TG\text{-}dq}\begin{bmatrix}\Delta i_d\\ \Delta i_q\end{bmatrix}=\begin{bmatrix}(CA^{-1})_{11} & (CA^{-1})_{12}\\ (CA^{-1})_{21} & (CA^{-1})_{22}\end{bmatrix}^{-1}\begin{bmatrix}\Delta i_d\\ \Delta i_q\end{bmatrix} \tag{9}$$

The matrix $\boldsymbol{C}$ in (9) is:

$$\boldsymbol{C}=\begin{bmatrix}1 & 0 & 0 & \cdots & 0\\ 0 & 1 & 0 & \cdots & 0\end{bmatrix} \tag{10}$$

The sequence impedance model of the turbo-generator is described in [22], and is expressed as:

$$Z_{TG\text{-}pn}=\begin{bmatrix}1 & 1\\ -j & -j\end{bmatrix}^{-1},\ Z_{TG\text{-}dq}\begin{bmatrix}1 & 1\\ -j & -j\end{bmatrix}=\begin{bmatrix}Z_{TG\text{-}pp} & Z_{TG\text{-}pn}\\ Z_{TG\text{-}np} & Z_{TG\text{-}nn}\end{bmatrix} \tag{11}$$

To validate the impedance model of the turbo-generator proposed in this study, a simulation model (shown in Fig. 7) is implemented in MATLAB/Simulink, initializing the output power to 300 MW. The model parameters are detailed in Tables III and IV. The theoretical model and frequency scanning results are shown in Fig. 8 which shows that the mathematical model of the equivalent impedance aligns with the scanning results, revealing resonance peaks at 27.6, 34.6, 38.2, and 43 Hz. Unlike the low-frequency oscillations observed in wind turbine mechanical structures [23], [24], the torsional vibration frequencies of turbo-generator shafting typically range between 5 and 50 Hz owing to the specific characteristics of these shafts. According to [25], the natural torsional vibration frequencies of the turbo-generator evaluated in this study are calculated as 7.0, 11.8, 15.4, and 22.4 Hz. Therefore, the electrical port's torsional vibration frequencies complement these, particularly around 50 Hz, correlating with the four mentioned resonance peaks.

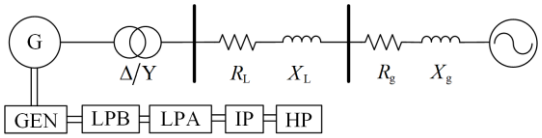

Fig. 7. Structure of turbo-generator grid-connected system.

TABLE III
PARAMETERS OF THE TURBO-GENERATOR

Symbol	Parameter	Value
u_N (kV)	Rated voltage of turbo-generator	22
P_N (MW)	Rated power of turbo-generator	600
x_d (p.u.)	D-axis synchronous reactance	1.65
x_q (p.u.)	Q-axis synchronous reactance	1.59
R_s (p.u.)	Stator resistance	0.0045
x_l (p.u.)	Leakage Reactance	0.14
x_f (p.u.)	Reactance of excitation winding	1.6286
x_D (p.u.)	Reactance of damping winding D	1.642
x_g (p.u.)	Reactance of damping winding g	1.8606
x_Q (p.u.)	Reactance of damping winding Q	1.5238
R_f (p.u.)	Resistors of excitation winding	0.001 152
R_D (p.u.)	Resistors of damping winding D	0.019 25
R_g (p.u.)	Resistors of damping winding g	0.008 84
R_Q (p.u.)	Resistors of damping winding Q	0.0139

TABLE IV
PARAMETERS OF THE GRID-SIDE SYSTEM

Symbol	Parameter	Value
N_1/N_2	Ratio of transformer	22/500
Z_t (Ω)	Impedance of transformer	0.25+j41.7
R_L (Ω)	Resistor of line	18.5
L_L (H)	Inductance of line	0.637
V_g (kV)	Network voltage	500
Z_g (Ω)	Internal grid impedance	0.5+j20.42

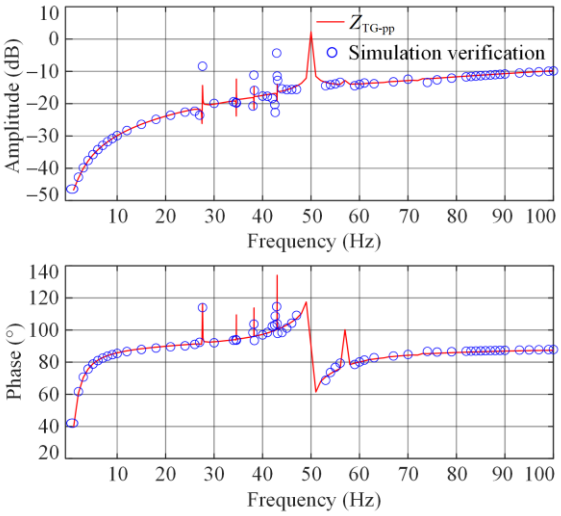

Fig. 8. Simulation and scanning verification of the turbo-generator impedance model.

Currently, the equivalent circuit impedance of synchronous generators is commonly employed as a substitute for turbo-generator impedance. The corresponding circuit is illustrated in Fig. 9 [18], [19], and its impedance model is expressed as:

$$Z_{TG} = R_a + s(L_a + L_\sigma) \tag{12}$$

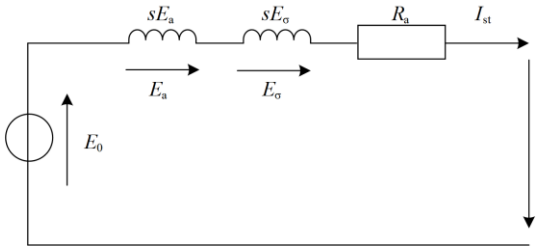

Fig. 9. Schematic diagram of the equivalent circuit of a synchronous generator.

The impedance model developed in this study is compared with the equivalent circuit impedance of a synchronous generator, as depicted in Fig. 10. As seen, significant differences exist between the two impedance curves near the electrical torsional vibration frequency. The impedance model of the turbo-generator established in this research exhibits a resonant peak near this frequency, indicating that shafting characteristics notably influence the impedance characteristics of the turbo-generator.

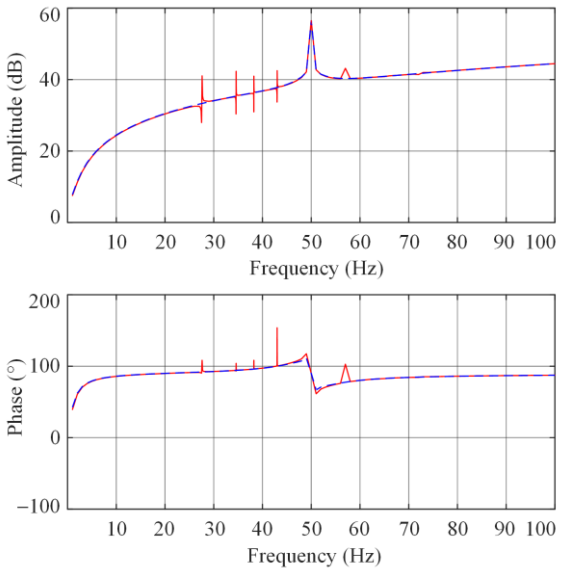

Fig. 10. Comparison of impedance circuits between synchronous generators and turbo-generators.

IV. SUB-SYNCHRONOUS OSCILLATION ANALYSIS OF TURBO-GENERATOR AND MMC-HVDC INTERCONNECTION SYSTEM

Based on the thermal power plant and nearby MMC-HVDC interconnection system structure in the Guangdong Province, impedance models for the turbo-generator, MMC, and transmission line are constructed.

Previous research indicates that neglecting frequency coupling effects in stability analysis can lead to inaccurate results [26], [27]. The relationship between voltage excitation and current response between the turbo-generator and the MMC-HVDC interconnection system is depicted in Fig. 11.

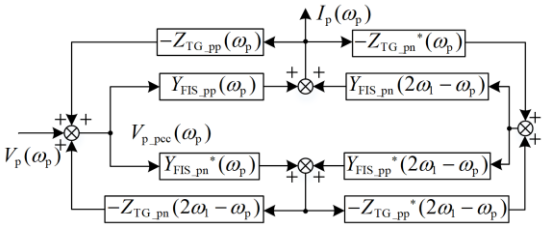

Fig. 11. Relationship diagram depicting voltage excitation and current response in the turbo-generator and MMC-HVDC interconnection system.

The expression for the equivalent impedance model of the MMC-HVDC interconnection system, accounting for frequency coupling effects, can be derived from Fig. 11, as shown in (A5). The Bode diagrams of the impedance models for the turbo-generator established in this study, the synchronous generator equivalent circuit model, and the MMC-HVDC interconnection system can be obtained, as illustrated in Fig. 12.

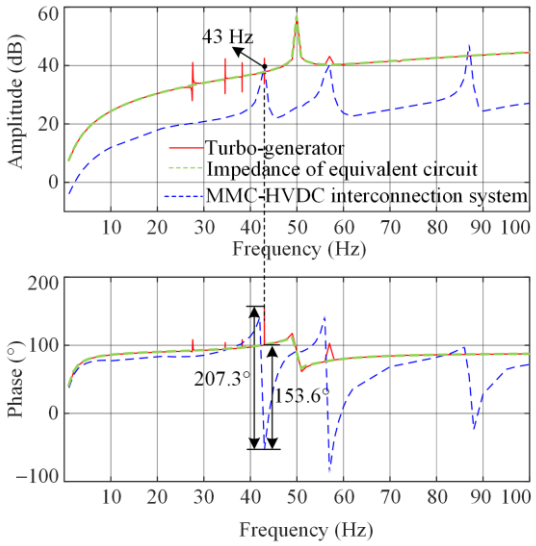

Fig. 12. Bode diagram of turbo-generator, synchronous generator equivalent circuit, and MMC-HVDC interconnection system impedance.

Figure 12 shows that the amplitude-frequency curves of the equivalent circuits for the turbo-generator, synchronous generator, and MMC-HVDC interconnection system intersect at 43 Hz. The phase difference between the turbo-generator impedance model developed in this paper and the MMC-HVDC interconnection system exceeds 180°, indicating the presence of sub-/super-synchronous oscillations in the system. In contrast, the phase difference between the equivalent circuit impedance model of the synchronous generator and the MMC-HVDC interconnection system is only 153.6°, indicating stable system without oscillation.

An electromagnetic transient model is constructed in MATLAB/Simulink to verify these findings. The current spectrum analysis results at the common connection point of the turbo-generator and the MMC-HVDC interconnection system, under oscillation conditions, are illustrated in Figs. 13 and 14.

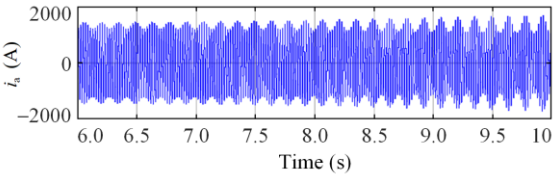

Fig. 13. Oscillation current waveform at the PCC of the turbo-generator and MMC-HVDC interconnection system (Phase A).

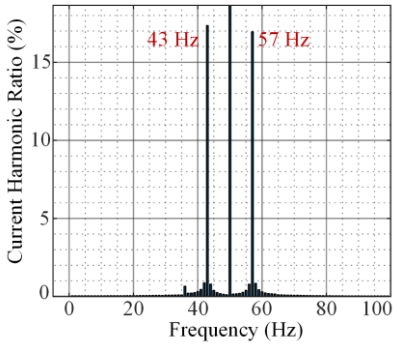

Fig. 14. Spectrum analysis of oscillating current.

Based on the current waveform and spectrum analysis results, the system current exhibits 43 Hz and 57 Hz harmonic components during the hybrid operation of the turbo-generator and the MMC-HVDC interconnection system. Over time, the current oscillates and diverges, leading to unstable system operation. The time-domain simulation results match the theoretical analysis using the developed turbo-generator impedance model, while contradict the analytical results based on the equivalent circuit impedance of the synchronous generator. This discrepancy arises because the impedance model based on the synchronous generator equivalent circuit primarily considers the electrical characteristics of the turbo-generator while neglecting the influence of shafting on impedance characteristics. Therefore, it fails to effectively analyze the oscillation risks near the natural frequency of the shafting system. This demonstrates the proposed model's ability to accurately assess stability in modern power systems incorporating power electronics and calculate sub-/super-synchronous oscillation frequencies.

V. Adaptive Virtual Damping Oscillation Suppression Strategy Based on Modulation Link and Case Analysis

Based on the analysis results in Section IV, it is evident that the combined operation of the turbo-generator and MMC-HVDC interconnection system may lead to sub-/super-synchronous oscillations. Therefore, this section proposes an adaptive virtual damping oscillation suppression strategy based on modulation link to suppress such oscillations.

The concept behind this control strategy is to introduce an equivalent virtual resistance into the bridge arm of the MMC converter by modifying the modulation signal input. This enhances system damping and effectively suppresses the oscillations. The controller structure diagram is depicted in Fig. 15, where u_{ref} is the initial voltage modulation signal input; i_{u} and i_{l} are the upper and lower bridge arm currents of the MMC converter; R_{V} is the virtual damping coefficient; and u_{refo} is the voltage modulation signal after incorporating virtual damping.

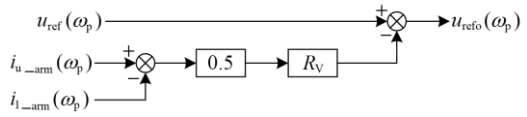

Fig. 15. Virtual damping control structure based on modulation link.

One of the key aspects of the virtual damping controller is to determine the virtual damping coefficient R_{V}, which reflects the equivalent increase in resistance

in the bridge arm. If the coefficient is too small, it will have negligible effect on suppressing the sub-synchronous oscillations, whereas if too large, it can impact the normal converter modulation process. Therefore, an adaptive algorithm is proposed to search for optimal virtual damping coefficients across varying operational conditions, as Fig. 16 showing its flowchart.

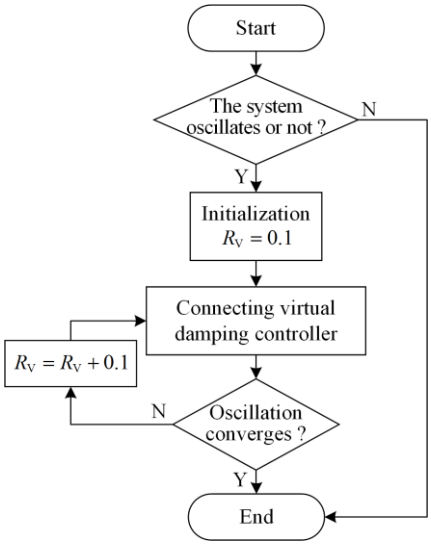

Fig. 16. Adaptive virtual damping oscillation suppression algorithm using modulation link.

Referring to the parameters in Section IV and increasing the output power of the turbo-generator to 600 MW, sub-/super-synchronous oscillations are induced in the system. Using the adaptive virtual damping coefficient acquisition algorithm depicted in Fig. 16, the obtained results are shown in Table V.

TABLE V
ADAPTIVE VIRTUAL DAMPING COEFFICIENT ACQUISITION

Iterations	Virtual damping coefficient	Phase Difference (°)	Phase margin (°)
1	0.1	240.67	−60.67
2	0.2	231.43	−51.43
3	0.3	221.22	−41.22
4	0.4	210.41	−30.41
5	0.5	199.6	−19.6
6	0.6	189.39	−9.39
7	0.7	180.18	−0.18
8	0.8	172.14	7.86

As seen from Table V, after eight iterations, the system oscillation current converges when $R_V = 0.8$, eliminating the sub-/super-synchronous oscillation. Subsequently, the controller is integrated into the system by setting the virtual damping coefficient R_V to 0.8. The impedance curves of the turbo-generator and the MMC-HVDC interconnection system before and after integrating the controller are shown in Fig. 17, and the intersection information at 43 Hz is summarized in Table VI.

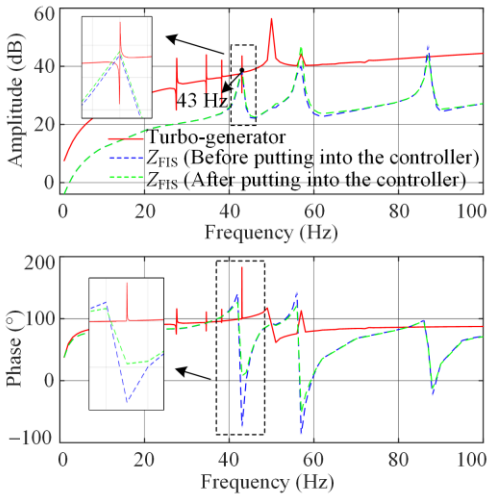

Fig. 17. Comparison of system impedance curves before and after virtual damping control implementation.

TABLE VI
INTERSECTION OF IMPEDANCE CURVES BEFORE AND AFTER VIRTUAL DAMPING CONTROLLER ACTIVATION

$R_V = 0.8$	Intersection frequency (Hz)	Impedance phase of Z_{TG} (°)	Impedance phase of Z_{FIS} (°)	Phase difference (°)
Before	43.0	179.8	−75.6	255.4
After	43.0	179.8	7.7	172.1

It is evident that in the frequency bands prone to oscillation (such as 43 Hz, 57 Hz, and 86 Hz), the impedance phase of the MMC-HVDC interconnection system noticeably increases, thereby enhancing the system's phase margin and stability. Consequently, the phase difference at the intersection is less than 180°, ensuring system stability without oscillation. The comparison of time-domain EMT simulation results before and after implementing the oscillation suppression strategy is illustrated in Fig. 18.

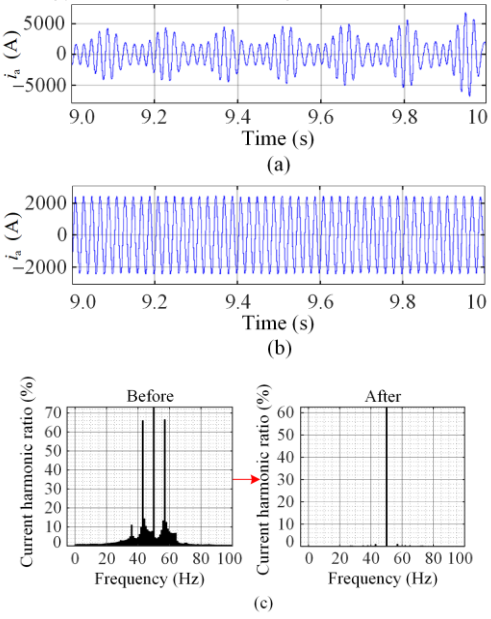

Fig. 18. Comparison of system current simulation results before and after virtual damping controller operation. (a) Before the virtual damping controller operates. (b) After the virtual damping controller operates. (c) FFT analysis results.

Figure 18 demonstrates that the system transitions from oscillation to a stable operation state after implementing the virtual damping controller. FFT analysis results align with the calculations from the adaptive virtual damping acquisition algorithm, validating the effectiveness of the designed adaptive virtual damping suppression strategy in this study.

To further demonstrate the effectiveness of vibration suppression, the controller is introduced into the system when the system starts oscillating (around 9 s), and the resulting trend of the system's oscillation current is depicted in Fig. 19. As seen, the system begins to diverge between 6–9 s, but gradual converges after applying the oscillation suppression strategy, demonstrating its effectiveness.

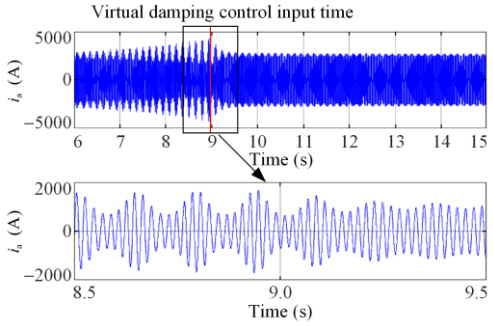

Fig. 19. System current waveform after the suppression strategy is applied at 9 s.

VI. Conclusion

In this study, an impedance model of the turbo-generator considering shafting characteristics is developed. Using a case study of oscillations at a thermal power plant and MMC-HVDC interconnection system in Guangdong province, China, the accuracy of the model proposed in this paper is confirmed, and an adaptive virtual damping oscillation suppression strategy is designed. The following conclusions are drawn.

1) The impedance model of the turbo-generator established in this paper is more accurate than the traditional model in the sub-synchronous frequency band.

2) The established impedance model can accurately analyze oscillation issues in modern power systems with power electronic devices.

3) An adaptive virtual damping suppression strategy based on a modulation link is designed, successfully suppressing the system's sub-synchronous oscillation.

Finally, the findings of this research provide both a model and practical insights for analyzing the stability of power systems incorporating turbo-generators and power electronics converters.

Appendix A

$$\begin{cases} Z_{\mathrm{FIS\_pp}}(\omega_\mathrm{p}) = \Big((Z_{\mathrm{MMC\_pp}}(\omega_\mathrm{p}) + Z_{\mathrm{T1}}(\omega_\mathrm{p}))\big/K_2^2 \,/\!/\, Z_{\mathrm{Tm}}(\omega_\mathrm{p}) + Z_{\mathrm{T2}}(\omega_\mathrm{p}) \to + \\ \qquad Z_{\mathrm{L}}(\omega_\mathrm{p}) /\!/ Z_{\mathrm{g}}(\omega_\mathrm{p}) + Z_{\mathrm{T2}}(\omega_\mathrm{p})\Big) /\!/ Z_{\mathrm{Tm}}(\omega_\mathrm{p}) + Z_{\mathrm{T1}}(\omega_\mathrm{p})\big/K_1^2 \\ Z_{\mathrm{FIS\_pn}}(\omega_\mathrm{p}) = Z_{\mathrm{MMC\_pn}}(\omega_\mathrm{p}) \end{cases} \tag{A1}$$

$$\begin{bmatrix} u_d \\ u_q \\ u_\mathrm{f} \\ 0 \\ 0 \\ 0 \end{bmatrix} = \begin{bmatrix} R_\mathrm{a} & 0 & 0 & 0 & 0 & 0 \\ 0 & R_\mathrm{a} & 0 & 0 & 0 & 0 \\ 0 & 0 & R_\mathrm{f} & 0 & 0 & 0 \\ 0 & 0 & 0 & R_\mathrm{D} & 0 & 0 \\ 0 & 0 & 0 & 0 & R_\mathrm{g} & 0 \\ 0 & 0 & 0 & 0 & 0 & R_\mathrm{Q} \end{bmatrix} \begin{bmatrix} -i_d \\ -i_q \\ i_\mathrm{f} \\ i_\mathrm{D} \\ i_\mathrm{g} \\ i_\mathrm{Q} \end{bmatrix} + \frac{s}{\omega_\mathrm{B}} \begin{bmatrix} \psi_d \\ \psi_q \\ \psi_\mathrm{f} \\ \psi_\mathrm{D} \\ \psi_\mathrm{g} \\ \psi_\mathrm{Q} \end{bmatrix} - \begin{bmatrix} \psi_q \\ -\psi_d \\ 0 \\ 0 \\ 0 \\ 0 \end{bmatrix} \omega_\mathrm{l} \tag{A2}$$

$$\begin{bmatrix} \psi_d \\ \psi_q \\ \psi_\mathrm{f} \\ \psi_\mathrm{D} \\ \psi_\mathrm{g} \\ \psi_\mathrm{Q} \end{bmatrix} = \begin{bmatrix} -x_d & 0 & x_{ad} & x_{ad} & 0 & 0 \\ 0 & -x_q & 0 & 0 & x_{aq} & x_{aq} \\ -x_{ad} & 0 & x_\mathrm{f} & x_{ad} & 0 & 0 \\ -x_{ad} & 0 & x_{ad} & x_\mathrm{D} & 0 & 0 \\ 0 & -x_{aq} & 0 & 0 & x_\mathrm{g} & x_{aq} \\ 0 & -x_{aq} & 0 & 0 & x_{aq} & x_\mathrm{Q} \end{bmatrix} \begin{bmatrix} i_d \\ i_q \\ i_\mathrm{f} \\ i_\mathrm{D} \\ i_\mathrm{g} \\ i_\mathrm{Q} \end{bmatrix} = X \begin{bmatrix} i_d \\ i_q \\ i_\mathrm{f} \\ i_\mathrm{D} \\ i_\mathrm{g} \\ i_\mathrm{Q} \end{bmatrix} \tag{A3}$$

$$\begin{cases} \Delta \boldsymbol{y} = \begin{bmatrix} \Delta i_d & \Delta i_q & \Delta i_\mathrm{f} & \Delta i_\mathrm{D} & \Delta i_\mathrm{g} & \Delta i_\mathrm{Q} & \Delta\alpha & \Delta\mu & \Delta T_2 & \Delta T_3 & \Delta T_4 & \Delta T_5 & \Delta\delta_1 & \Delta\delta_2 & \Delta\delta_3 & \Delta\delta_4 & \Delta\delta_5 & \Delta\omega_1 & \Delta\omega_2 & \Delta\omega_3 & \Delta\omega_4 & \Delta\omega_5 \end{bmatrix}^\mathrm{T} \\ \Delta \boldsymbol{u} = \begin{bmatrix} \Delta u_d & \Delta u_q & 0 & \cdots & 0 \end{bmatrix}^\mathrm{T} \end{cases} \tag{A4}$$

$$\begin{cases} Y_{\mathrm{FIS\_inv}}(\omega_\mathrm{p}) = I_\mathrm{p}(\omega_\mathrm{p})\big/V_{\mathrm{p\_pcc}}(\omega_\mathrm{p}) = Y_{\mathrm{FIS\_pp}}(\omega_\mathrm{p}) + Y_C(\omega_\mathrm{p}) \\ Y_C(\omega_\mathrm{p}) = \dfrac{-\left[Y_{\mathrm{FIS\_pp}}(\omega_\mathrm{p}) Z^*_{\mathrm{TG\_pn}}(\omega_\mathrm{p}) + Y^*_{\mathrm{FIS\_pn}}(\omega_\mathrm{p}) Z^*_{\mathrm{TG\_pp}}(2\omega_\mathrm{l} - \omega_\mathrm{p})\right] Y^*_{\mathrm{FIS\_pp}}(2\omega_\mathrm{l} - \omega_\mathrm{p})}{1 + Y_{\mathrm{FIS\_pn}}(2\omega_\mathrm{l} - \omega_\mathrm{p}) Z^*_{\mathrm{TG\_pn}}(\omega_\mathrm{p}) + Y^*_{\mathrm{FIS\_pp}}(2\omega_\mathrm{l} - \omega_\mathrm{p}) Z^*_{\mathrm{TG\_pp}}(2\omega_\mathrm{l} - \omega_\mathrm{p})} \\ Z_{\mathrm{FIS\_inv}}(\omega_\mathrm{p}) = 1\big/Y_{\mathrm{FIS\_inv}}(\omega_\mathrm{p}) \end{cases} \tag{A5}$$

ACKNOWLEDGMENT

Not applicable.

AUTHORS' CONTRIBUTIONS

Jialong Li: conceptualization, data curation, formal analysis, methodology, software, and writing-original draft. Xinyu Lu: methodology and software. Xiong Du: project administration, resources, supervision, writing-review, and editing. Junliang Liu: project administration, resources, writing-review, and editing. Lijuan Fan: writing-review and editing. All authors read and approved the final manuscript.

FUNDING

This work is supported by the Key Project of National Natural Science Foundation of China (No. 51937001, No. 52125704, and No. 52307192).

AVAILABILITY OF DATA AND MATERIALS

Not applicable.

DECLARATIONS

Competing interests: The authors declare that they have no known competing financial interests or personal relationships that could have appeared to influence the work reported in this article.

AUTHORS' INFORMATION

Jialong Li graduated from the School of Electrical Engineering of Chongqing University and received his Bachelor's and Master's degrees in 2021 and 2024 respectively.

Xinyu Lu graduated from the School of Electrical Engineering of Chongqing University with a Master's degree. Her research direction is stability analysis of power electronic systems.

Xiong Du received his Bachelor's, Master's and Doctor's degrees from Chongqing University in 2000, 2002 and 2005 respectively. He was a lecturer at Chongqing University from 2005 to 2007 and a visiting scholar at the Department of Electrical Engineering at Rensselaer Polytechnic Institute from 2007 to 2008. He was an associate professor at Chongqing University from 2007 to 2010 and a professor at Chongqing University from 2010 to now. His research interests include HVDC system stability, new energy grid-connected system stability and power electronics equipment reliability.

Junliang Liu graduated from the School of Electrical Engineering of Chongqing University with a doctorate degree in 2022, and now works as a research assistant in the School of Electrical Engineering of Chongqing University. His research direction is stability analysis of power electronic systems.

Lijuan Fan graduated from the Department of Electrical Machinery of Tsinghua University with a Master's degree in 2010. Now she is working at System Research Institute of CSG Electric Power Research Institute, engaged in the research of AC and DC power system safety and stability, harmonics and resonance, and electromagnetic transient simulation of power systems.

REFERENCES

[1] H. Zhang, M. M. Belhaouane, and F. Colas *et al*., "On comprehensive description and analysis of MMC control design: simulation and experimental study," *IEEE Transactions on Power Delivery*, vol. 36, no. 1, pp. 244-253, Feb. 2021.

[2] Y. Song, Y. Luo, and X. Xiong, "Loss distribution analysis and accurate calculation method for bulk-power MMC," *Protection and Control of Modern Power Systems*, vol. 8, no. 1, pp. 1-15, Jan. 2023.

[3] J. Xu, A. M. Gole, and C. Zhao, "The use of averaged-value model of modular multilevel converter in DC grid," *IEEE Transactions on Power Delivery*, vol. 30, no. 2, pp. 519-528, Apr. 2015.

[4] Y. Zhao, B. Zheng, and Z. He, "The control mode and operating performance of Nanhui VSC-HVDC demonstration project," *Southern Power System Technology*, vol. 6, no. 6, pp. 6-10, Jun. 2012. (in Chinese)

[5] E. Pan, B. Le, and N. Mei *et al*., "System design of ±420 kV Chongqing-Hubei back-to-back HVDC project of China," *Automation of Electric Power Systems*, vol. 45, no. 5, pp. 175-183, Mar. 2021. (in Chinese)

[6] X. Du, Q. Guo, and Y. Wu *et al*., "Research on control system structure and coordination control strategy for Zhangbei demonstration project of MMC-HVDC grid," *Power System Protection and Control*, vol. 48, no. 9, pp. 164-173, May 2020. (in Chinese)

[7] M. Bahrman, E.V. Larsen, and R. J. Piwko *et al.*, "Experience with HVDC-Turbine-Generator Torsional Interaction at Square Butte," *IEEE Transactions on Power Apparatus and Systems*, vol. PAS-99, no. 3, pp. 966-975, May 1980.

[8] Y. Liu, X. Zhou, and Q. Chen *et al*., "Harmonic state space based impedance modeling and virtual impedance based stability enhancement control for LCC-HVDC systems," *Journal of Modern Power Systems and Clean Energy*, vol. 12, no. 1, pp. 287-298, Jan. 2024.

[9] P. Zhang and T. Bi, "Mechanism analysis of large disturbance risk of subsynchronous oscillation caused by HVDC," *Proceedings of the CSEE*, vol. 36, no. 4, pp. 961-968, Feb. 2016. (in Chinese)

[10] P. Zhang, T. Bi, and Q. Yang *et al*., "Research on subsynchronous oscillation of parallel connected generators with torsional frequencies," *Proceedings of the CSEE*, vol. 35, no. 20, pp. 5181-5187, Oct. 2015. (in Chinese)

[11] J. Sun, "Impedance-based stability criterion for grid-connected inverters," *IEEE Transactions on Power Electronics*, vol. 26, no. 11, pp. 3075-3078, Nov. 2011.

[12] Z. Yao, Q. Zhang, and P. Chen *et al.*, "Research on fault diagnosis for MMC-HVDC systems," *Protection and Control of Modern Power Systems*, vol. 1, no. 1, pp. 1-7, Jun. 2016.

[13] Z. Fu, W. Sima, and M. Yang *et al*., "A mutual-inductance-type fault current limiter in MMC-HVDC systems," *IEEE Transactions on Power Delivery*, vol. 35, no. 5, pp. 2403-2413, Oct. 2020.

[14] Q. Hao, Z. Li, and C. Yue *et al.*, "Small-signal model and dynamics of MMC-HVDC grid under unbalanced grid conditions," *IEEE Transactions on Power Delivery*, vol. 36, no. 5, pp. 3172-3184, Oct. 2021.

[15] X. Chen, Y. Wang, and C. Gong *et al*., "Overview of stability research for grid-connected inverters based on impedance analysis method," *Proceedings of the CSEE*, vol. 38, no. 7, pp. 2082-2094, Apr. 2018. (in Chinese)

[16] A. Tabesh and R. Iravani, "On the application of the complex torque coefficients method to the analysis of torsional dynamics," *IEEE Transactions on Energy Conversion*, vol. 20, no. 2, pp. 268-275, Jun. 2005.

[17] Y. Zhang, X. Chen, and J. Sun, "Sequence impedance modeling and analysis of MMC in single-star configuration," *IEEE Transactions on Power Electronics*, vol. 35, no. 1, pp. 334-346, Jan. 2020.

[18] W. Zhao, S. Wang, and X. Sun *et al.*, "Impedance modeling and stability research of hybrid parallel system with synchronous generator and inverters," in *Proceedings of the 2018 IEEE International Power Electronics and Application Conference and Exposition (PEAC)*, Shenzhen, China, Nov. 2018, pp. 1-6.

[19] Y. Gu, Y. Li, and Y. Zhu *et al.*, "Impedance-based whole-system modeling for a composite grid via embedding of frame dynamics," *IEEE Transactions on Power Systems*, vol. 36, no. 1, pp. 336-345, Jan. 2021.

[20] J. Khazaei, M. Beza, and M. Bongiorno, "Impedance analysis of modular multi-level converters connected to weak AC grids," *IEEE Transactions on Power Systems*, vol. 33, no. 4, pp. 4015-4025, Jul. 2018.

[21] IEEE Subsynchronous Resonance Working Group, "First benchmark model for computer simulation of subsynchronous resonance," *IEEE Transactions on Power Apparatus and Systems*, vol. PAS-96, no. 5, pp. 1566-1572, Oct. 1977.

[22] A. Rygg, M. Molinas, and C. Zhang *et al.*, "A modified sequence-domain impedance definition and its equivalence to the *dq*-domain impedance definition for the stability analysis of AC power electronic systems," *IEEE Journal of Emerging and Selected Topics in Power Electronics*, vol. 4, no. 4, pp. 1383-1396, Dec. 2016.

[23] X. Gao, Z. Xie, and M. Li *et al*., "Analysis and mitigation of electromechanical oscillations in drivetrain for hybrid synchronization control of DFIG-based wind turbines," *IEEE Transactions on Power Electronics*, vol. 39, no. 3, pp. 3002-3013, Mar. 2024.

[24] X. Zhang, W. He, and J. Hu, "Impact of inertia control of DFIG-based WT on torsional vibration in drivetrain," *IEEE Transactions on Sustainable Energy*, vol. 11, no. 4, pp. 2525-2534, Oct. 2020.

[25] IEEE Subsynchronous Resonance Working Group, "Terms, definitions and symbols for subsynchronous oscillations," *IEEE Transactions on Power Apparatus and Systems*, vol. 104, no. 6, pp. 1326-1334, Mar. 1980.

[26] X. Zhou, X. Du, and G. Wang *et al*., "Frequency coupling mechanism analysis and stability judgement for three-phase grid-connected inverter," *Automation of Electric Power Systems*, vol. 42, no. 18, pp. 57-63, Sept. 2018. (in Chinese)

[27] C. Du, X. Du, and C. Tong, "SSR stable wind speed range quantification for DFIG-based wind power conversion system considering frequency coupling," *IEEE Transactions on Sustainable Energy*, vol. 14, no. 1, pp. 125-139, Jan. 2023.